Lawrence Berkeley National Laboratory

Title
Temperature, humidity and air flow in the emplacement drifts using convection and dispersion transport models

Permalink
https://escholarship.org/uc/item/5v60g37v

Author
Danko, G.

Publication Date
2010-09-07

Peer reviewed

TEMPERATURE, HUMIDITY AND AIR FLOW IN THE EMPLACEMENT DRIFTS USING CONVECTION AND DISPERSION TRANSPORT MODELS

G. Danko[1], J. Birkholzer[2], D. Bahrami[1], N. Halecky[2]

[1]Department of Mining Engineering, University of Nevada Reno

[2]Lawrence Berkeley National Laboratory (LBNL)

Person to whom proofs and page charge are to be sent:

Dr. George Danko

Mailing Address:

Mackay School of Earth Sciences and Engineering,

University of Nevada, Reno

1664 North Virginia Street, Mail stop 173

Reno, NV 89557

Phone: (775)784-4284

Fax: (775)784-4284

Email: danko@unr.edu

ABSTRACT

A coupled thermal-hydrologic-airflow model is developed, solving for the transport processes within a waste emplacement drift and the surrounding rockmass together at the proposed nuclear waste repository at Yucca Mountain. Natural, convective air flow as well as heat and mass transport in a representative emplacement drift during post-closure are explicitly simulated, using the MULTIFLUX model. The conjugate, thermal-hydrologic transport processes in the rockmass are solved with the TOUGH2 porous-media simulator in a coupled way to the in-drift processes. The new simulation results show that large-eddy turbulent flow, as opposed to small-eddy flow, dominate the drift air space for at least 5000 years following waste emplacement. The size of the largest, longitudinal eddy is equal to half of the drift length, providing a strong axial heat and moisture transport mechanism from the hot to the cold drift sections. The in-drift results are compared to those from simplified models using a surrogate, dispersive model with an equivalent dispersion coefficient for heat and moisture transport. Results from the explicit, convective velocity simulation model provide higher axial heat and moisture fluxes than those estimated from the previously published, simpler, equivalent-dispersion models, in addition to showing differences in temperature, humidity and condensation rate distributions along the drift length. A new dispersive model is also formulated, giving a time- and location-variable function that runs generally about ten times higher in value than the highest dispersion coefficient currently used in the Yucca Mountain Project as an estimate for the equivalent dispersion coefficient in the emplacement drift. The new dispersion coefficient variation, back-calculated from the convective model, can adequately describe the heat and mass transport processes in the emplacement drift example.

KEYWORDS

I. INTRODUCTION

A numerical simulation study is conducted to understand the coupling between thermo-hydrological-airflow processes (THA) (including air and vapor movement) in the in-drift, near-field, and mountain-scale systems at Yucca Mountain (YM). Specific aims are (1) to configure, test, and verify a novel, efficient, numerical-computational, coupled, THA model; and (2) to evaluate, at different stages after waste emplacement, the coupled, in-drift heat, moisture, and air flow transport with evaporation, condensation, and seepage of water into drifts from the near-field rockmass that is embedded in a mountain-scale geologic unit. These objectives are met by applying a multi-scale modeling approach that (1) integrates in-drift and in-rock process models, with new laminar or turbulent air flow components, in a consistent and transparent manner; and (2) allows for studying the storage environment in various emplacement drifts with refined model assumptions. The multi-scale, in-rock and in-drift model domains, shown in Figure 1, are the same as the ones used in a previous study [1]. The in-rock model domain includes the near-field as well as far-field rockmass around an emplacement drift, large-enough in every direction to encapture the heat and moisture transport processes.   The in-drift model domain includes the waste packages (WP), the drip shields, and the drift airspace.

The key elements of the new modeling approach are (1) the separation of the rockmass model-element of the host geological formation from the in-drift model-element of the engineered nuclear waste emplacement system; (2) the detailed, general model solution of the rockmass with a porous-media, thermal-hydrologic model, in this case, TOUGH2 [2]; (3) the detailed model solution of the internal components of the emplacement drift and the air space with a integrated-parameter CFD (Computational Fluid Dynamics) model; and (4) the dynamic re-coupling of the separate tasks (2) and (3) iteratively at each time instant and boundary element at the drift wall. All key model-elements are simultaneously applied during simulation within the MULTIFLUX (MF) framework [3], a software

developed at the University of Nevada, Reno (UNR) for solving coupled heat, mass, and air flow modeling tasks. The solutions to the separate tasks are accomplished by a new way, allowing for efficient and dynamic re-coupling, by using the NTCF (Numerical Transport Code Functionalization) technique [4].

In previous work, the solution for the coupled system comprising the rockmass and waste emplacement drift domains was approximated within one monolithic domain as a classic solution to the heat and mass transport problem using a porous-media model, either TOUGH2 [2] or NUFT [5]. Bechtel SAIC Company [6] developed such an approximate model for a three-dimensional (3D) panel by representing a full emplacement drift and the surrounding rockmass. The heat and moisture transport processes in both the rockmass and the air space in the emplacement drifts were modeled with NUFT. The in-drift transport processes were approximated with an equivalent dispersion model, allowing for heat and moisture flow, driven by temperature and vapor concentration gradients within the in-drift model domain. In the latest model revision (Rev 03) [6], the axial dispersion coefficient was taken as 1000 times the molecular, binary diffusion coefficient for still air. This gave a temperature-dependent dispersion coefficient of around 0.025 m^2/s in value, much lower than the value of 0.1 m^2/s reported as the highest value for early time periods for Yucca Mountain [7]. Birkholzer et al. [8, 9] further improved the monolithic modeling concept using TOUGH2. Monolithic models, however, can only approximate the air flow field and its effects on heat and moisture transport within the air space of the emplacement drift by equivalent dispersion. Air flow during the first few thousand of years forms dominantly turbulent, recirculatory patterns, and the flow regime exceeds the modeling capabilities of the porous-media codes, all involving only the law of Darcy flows. In addition, the contrast in permeabilities between the in-rock and in-drift model domains are simply too large (of the order of 10^{11}) to be solvable within one numerical solution framework. For example, the average permeability in the

fractured rockmass at YM is on the order of 10^{-12} m^2 [6], while permeability, k, of the open air space in the emplacement drift is as high as 10^{-1} m^2, assuming Darcy flow and using the $k=r^2/8$ formula where r is the radius of the drift.

Solutions for just the in-drift environment, separated from the other model-elements of the porous rock, have also been published. Bechtel SAIC Company [7] solved for the temperature and humidity distribution in the in-drift emplacement system using a two-step approach. First, in a 70 m long section of the in-drift domain, the 3D heat transport and air flow were modeled using a commercial CFD model, FLUENT [7]. The CFD model was coupled to a hollow rock cylinder surrounding the emplacement drift, in which heat transport by conduction was assumed, driven by a prescribed temperature boundary condition at some distance in the rock wall. The solution excluded moisture transport, and was used to evaluate an equivalent, effective dispersion coefficient in the drift air space under the single driving force of temperature-induced buoyancy effects. In a second step, the moisture transport was modeled in an entire emplacement drift, using a separate, integrated-parameter network model that used the dispersive transport coefficients derived from the FLUENT-based CFD model. In this separate moisture transport model, the availability of moisture was assumed due to 100% relative humidity at the drift wall along the emplacement drift. While this combined solution included some simulated thermal interactions between the rockmass and in-drift domains, it did not consider the diffusive and convective interactions regarding moisture transport. Passive vapor transport from an impermeable surface at saturated vapor pressure may be either higher or lower relative to the real moisture flux, which is generally comprised of two components: (1) convective flux, which may include superheated steam, driven by the total pressure gradient; and (2) diffusive flux, driven by the humidity concentration gradient. Even the moisture flow direction at a drift surface element cannot be known without a coupled model.

Hao et. al [10] developed a double-diffusion CFD solver for a two-dimensional slice normal to the drift axis of an emplacement drift, also with prescribed boundary conditions, but without being coupled to the rockmass and without iterating between the two different, but conjugate model domains. However, the results from the double-diffusion CFD model pointed out the importance of taking into account both temperature and humidity variations in the air space since both affected the buoyancy driving force for air circulation. The findings of Hao et. al [10], although not directly applicable to a three-dimensional drift example, render previous CFD models of air circulation with only temperature driving force questionable. Neither the FLUENT-based CFD model for an emplacement drift section [7], nor the previous, much simpler model used for explaining the air circulation and natural convection in a two-dimensional section of a scaled laboratory experiment using an ANSYS-FLOTRAN CFD calculation and dry heat transfer model [11] included the second driving force due to moisture content variation in the air space. In comparison, the integrated-parameter CFD model in MF applies the double driving force, due to both temperature and humidity variation in a three-dimensional air space domain of a full emplacement drift.

In previous work, we have conducted numerical tests with the fully coupled MF framework including comparison with published results obtained using an alternative, albeit simplified model [8,9] involving a large model domain. Comparisons showed good agreement between the results from the monolithic model [8,9] and those from the coupled MF model, configured with equivalent dispersion transport processes along the axial direction of the emplacement drift [12]. The current paper goes beyond the previous MF model configurations of equivalent dispersion. The new software and model version of MF allows for explicit calculation of the velocity field in the emplacement drift, determining the natural air movement driven by temperature and humidity variations within the air space, and the resultant heat and moisture transport processes due to natural convection during post-closure. The paper

describes the new results involving large-eddy, laminar or turbulent heat, moisture and air flows and discuss these with some of the early results from alternative solutions.

A MULTI-SCALE, COUPLED NUMERICAL-COMPUTATIONAL MODEL

Model Concept

The numerical simulator MF Version 5.0 is used in the evaluation of three different in-drift transport approaches, each utilizing different transport mechanisms. In the first approach, called Case A, the axial transport is represented by an equivalent dispersion process using a constant dispersion coefficient of 0.1 m^2/s taken from published results [7] and constant convective air flow components in the vertical cross-sections, also calculated based on published results [7]. In the second approach, called Case B, the coupled in-drift airflow field, caused by natural convection, is explicitly and iteratively solved within MF, using its three-dimensional integrated-parameter solver for the Navier-Stokes equation. The natural air flow field is simultaneously used for a direct simulation of the axial heat and moisture fluxes in Case B. In order to prepare for Case C, the natural airflow field is utlilized to determine an effective, equivalent dispersion coefficient that can be substituted in the model similar to the first approach in Case A. For the substitution in Case C, the equivalent, axial dispersion coefficient distribution is back-calculated from the velocity field as a function of space and time, then imported into a predictive model of an axial dispersion type with variable axial dispersion coefficient. The dispersion model in Case C thus uses an effective, equivalent representation of the convective heat and moisture transport in axial direction with a time- and space dependent dispersion coefficient assigned at a given axial location in the drift. Two different dispersion coefficients may be used, one under, and one over the drip shield air space in each drift cross section. The WPs are modeled as individual heat sources at with an initial line load of 1.45 KW/m along the heated section of the emplacement drift. The initial load decreases

exponentially with time as a result of radioactive decay. During the 50-year preclosure period following waste emplacement, forced ventilation removes the majority of the heat from the repository, ensuring that the temperature increase is moderate and access to the drifts is still possible.

Thermal-hydrologic Model of the Rockmass

The multi-scale rockmass model is identical to that of previous studies [1, 12]. The rockmass surrounds a representative drift in the middle of an emplacement panel. The length of the drift is 760 m with two 80 m long end sections where no waste is emplaced. The length of the unheated sections are kept at 80 m, the same length used by Birkholzer et al [8, 9] in order to evaluate agreements and/or differences caused by transport model components instead of arrangement geometry. It has been pointed out before by Danko et al [12] that the axial moisture transport and the humidity in the emplacement drift are quite sensitive to the length of the unheated sections. The unheated drift sections are connected to the undisturbed and also unheated edges, which provide a dominantly conductive heat sink to the heated portion of the rockmass around the center of the emplacement drift. This arrangement, described in [12], manifests a strongly 3-D temperature field in and around the drift with cooler temperatures around the drift ends. Likewise, the representative NTCF model, a surrogate model using response functions based on the TOUGH2 thermal-hydrologic porous-media code, is also used unchanged. Not revising the NTCF model provides for an un-biased comparison between Cases A through C regarding the effects of in-drift model type selection.

It is sufficient to refer to a previous study [12] for the NTCF model representing the rockmass response. Along the length of the drift, 44 individual mountain-scale divisions are applied. The relationships between the set of input T, P, and output qh, qm temporal variations for each drift section

define the corresponding dynamic, rockmass model for heat and moisture according to the following matrix equations[12]:

$$qh = qh^c + hh \cdot \left(T - T^c\right) + \langle T \rangle \cdot hm \cdot \left(P - P^c\right) \tag{1}$$

$$qm = qm^c + mh \cdot \left(T - T^c\right) + \langle T \rangle \cdot mm \cdot \left(P - P^c\right) \tag{2}$$

Where qh and qm are NTCF output heat and moistures fluxes,

    hh and hm are NTCF dynamic admittance matrices for heat,

    hm and mm are NTCF dynamic admittance matrices for moisture,

    T is input temperature,

    P is input vapor pressure, and

    superscript c refers to central boundary conditions.

The hh, hm, mh, and mm dynamic admittance matrices are identified based on Eqs (1) and (2) by fitting qh and qm to TOUGH2 data. The NTCF model identification method follows the technique described in [4]. The model for each drift-section perfectly reproduces qh^c and qm^c, the central output fluxes from TOUGH2, for $T=T^c$ and $P=P^c$, the central input boundary conditions.

Other T and P input variations can produce outputs from the NTCF model for qh and qm without actually re-running TOUGH2. For the coupled in-rock and in-drift model, 454 drift-scale NTCF models are generated from the mountain-scale NTCF models by scaling, following the technique used in [12].

CFD Models for Heat, Moisture, and Air Flow Transport in the Emplacement Drift

The integrated-parameter, in-drift CFD model domain is also identical to that in a previous study [12]. However, the heat, mass, and air flow transport connections within the emplacement drift are re-configured according to the three different model approaches in Cases A through C.

In all cases, the energy balance equation in the CFD model of MF is used in a simplified form, as follows, for an *x*-directional flow with v_i velocity in a flow channel of cross section *dy* by *dz* (and with no convective heat transport in *y* and *z* directions while considering the *x*-directional flow):

$$\rho c \frac{\partial T}{\partial t} + \rho c v_i \frac{\partial T}{\partial x} = \rho c a \frac{\partial^2 T}{\partial x^2} + \rho c a \frac{\partial^2 T}{\partial y^2} + \rho c a \frac{\partial^2 T}{\partial z^2} + \dot{q}_h \tag{3}$$

In Eq. (3), ρ and *c* are density and specific heat of moist air, respectively; *a* is the molecular or eddy thermal diffusivity for laminar or turbulent flow; and $\dot{q}_h$ is the latent heat source or sink for condensation or evaporation. In Case A, the thermal diffusivity, *a*, is equated with the constant dispersion coefficient of 0.1 m^2/s in axial direction, while the molecular diffusivity is used in all other directions, since enhanced transport in the vertical cross sections is represented by convections with an imported velocity field [12]. In Case B, *a* equals the molecular diffusivity in all directions, as moisture transport by convective air flow is explicitly modeled. In Case C, *a* is equated with the variable, effective dispersion coefficient in the axial direction, and with the molecular diffusivity in all other directions. The second and the third terms on the right-hand-side of Eq. (3) represent heat conduction (or effective heat conduction) in the *y* and *z* directions, normal to the x axis of the flow channel; these terms are substituted with expressions for transport connections using heat transport coefficients for

flow channels bounded by solid walls. Eq. (3) is discretized and solved numerically and simultaneously along all flow channels for the temperature field T in MF [3].

The simplified moisture transport convection-diffusion equation in the CFD model of MF is similar to Eq. (3) as follows:

$$\rho\frac{\partial \omega}{\partial t} + \rho v_i \frac{\partial \omega}{\partial x} = \rho D \frac{\partial^2 \omega}{\partial x^2} + \rho D \frac{\partial^2 \omega}{\partial y^2} + \rho D \frac{\partial^2 \omega}{\partial z^2} + qc + qs + qm \qquad (4)$$

Where ω is the vapor mass fraction $\omega = \dfrac{P \cdot Ra/Rv}{Pb - (1 - Ra/Rv) \cdot P}$

x, y, z are Cartesian coordinates,

t is time

P is partial vapor pressure,

Pb is air total, barometric pressure,

Ra is gas constant for dry air,

Rv is gas constant for water vapor,

ρ is density of moist air,

D is the molecular or eddy diffusivity for vapor for laminar or turbulent flow,

qc is the moisture source or sink due to condensation or evaporation at node i, and

qs is the vapor flux source or sink at node i in superheated steam form.

D is calculated from the thermal diffusivity, a, which is substituted specifically according to Cases A, B, or C, as explained for Eq. (3).

The Navier-Stokes momentum balance equation for 3D flow of the bulk air-moisture mixture is used as follows, following [13]:

$$\rho\left(\frac{\partial v_x}{\partial t} + \mathbf{v} \cdot \nabla v_x\right) = \rho g_x - \frac{\partial Pb}{\partial x} + F_x \tag{5a}$$

$$\rho\left(\frac{\partial v_y}{\partial t} + \mathbf{v} \cdot \nabla v_y\right) = \rho g_y - \frac{\partial Pb}{\partial y} + F_y \tag{5b}$$

$$\rho\left(\frac{\partial v_z}{\partial t} + \mathbf{v} \cdot \nabla v_z\right) = \rho g_z - \frac{\partial Pb}{\partial z} + F_z \tag{5c}$$

Where v_x, v_y, v_z are velocity components of vector v,

g_x, g_y, g_z are gravitational forces which include buoyancy in x, y, and z directions, and

F_x, F_y, F_z are viscous terms.

The viscous terms in Eqs. (5a-c) are expressed with the viscous normal-stress $(\sigma)_v$ and shear-stress (τ) components as follows [13]:

$$F_x = \frac{\partial(\sigma_{xx})_v}{\partial x} + \frac{\partial \tau_{yx}}{\partial y} + \frac{\partial \tau_{zx}}{\partial z} \tag{6a}$$

$$F_y = \frac{\partial \tau_{xy}}{\partial x} + \frac{\partial(\sigma_{yy})_v}{\partial y} + \frac{\partial \tau_{zy}}{\partial z} \tag{6b}$$

$$F_x = \frac{\partial \tau_{xz}}{\partial x} + \frac{\partial \tau_{yz}}{\partial y} + \frac{\partial(\sigma_{zz})_v}{\partial z} \tag{6c}$$

The viscous force terms in Eqs. (6a-6c) are integrated along the grid lines of the flow channels and expressed as a function of the convective air flow components in the emplacement drift [3].

The integrated-parameter CFD model approach allows for reducing the number of discretization elements in the computational domain [12]. MF allows for defining connections between integrated volumes, applying direct heat and moisture transport relations between them. The current, integrated-parameter CFD model in the drift applies 18x454=8172 nodes for the heat, and the same number of

nodes for the moisture transport as well as for air flow transport. Each WP is represented by two nodes [12], with one additional node for the gap between neighboring containers. CFD nodes are in the airway along four longitudinal lines in a half-cross-section of the drift on either side of the symmetry line: (1) close to the floor; (2) close to the drip shield; (3) close to the drift wall at mid-height; and (4) above the drip shields, with 454 nodes on each line [12]. The drift wall is assumed to be separated from the rock with a 10^{-5} m-thick still air layer representing the rock-air interface, and acting as a coupling layer of insignificant resistance to transport of heat and moisture. Both the drift wall and the thin coupling layer are represented by 454 nodes each along three longitudinal lines along the drift length: at the invert, sidewall, and roof. The airspace under the drip shields is also modeled by four lines, each having 454 nodes. Half of the drip shield on either side of the symmetry line is represented by four nodes defining four lines, two on the top and two on the side. Each air space, one above and one under the drip shield, also includes one steam transport line. Heat and moisture transport are modeled using heat and moisture transport coefficients at the WP, drift wall, and at each side of the drip shield. 3D thermal radiation between solid surfaces is also included in the CFD model.

Natural air flow is considered due to the local temperature differences in each of Cases A through C in the vertical planes normal to the drift axis. In Cases A and C, these transversal velocities are imported from literature [7] by taking them at a constant value of 0.1 m/s, while the mean axial air flow is assumed to be zero, eliminating convection, in lieu of a dispersion transport model. In Case B, the radial, tangential, and axial velocity components are all explicitly modeled and calculated in MF.

Coupled In-rock NTCF and In-drift CFD Models

The NTCF (approximating the rockmass response) and CFD models are coupled on the rock-air interface by MF until the heat and moisture fluxes are balanced at the common surface temperature and

13

partial vapor pressure at each surface node and time instant. Two iteration loops are used to balance the in-rock and in-drift transport processes on the rock-air interface:

1. Heat flow balance iteration between the NTCF and airway CFD models for each time division.

2. Moisture flow balance iteration between the NTCF and airway CFD models for each time division.

In Case B, an outer iteration loop is used to determine the natural air flow field in the closed air space of the emplacement drift. For each set of balanced results from iterations 1 and 2, the air flow velocity field is solved based on the new, updated temperature and vapor pressure distribution in an outside balance loop until no significant change is observed between consecutive iterations. The convergence of the iteration for the velocity distribution in the natural air flow field is discussed in another paper [14]. Suffice to recite that it is no small accomplishment to make this iteration converge, considering that the result is the solution of a set of nonlinear equations with several thousands of unknown variables.

The simulation results obtained from the CFD model elements for each of the Cases A through C are temperature, relative humidity, and water condensate variations within the emplacement drift, including their distributions on the drift wall boundary. Relative humidity is defined as the ratio of partial vapor pressure, P, to barometric pressure, Pb. In the current study, we focus on these in-drift conditions. In other studies, the main focus may be directed to the processes in the rockmass and not in the drift, such as in [8,9]. Temperature, humidity, and moisture flow distributions in the rockmass, already coupled to the in-drift processes, are given by the TOUGH2 porous-media model. Read-out of saturation and/or moisture flow results in the rockmass from TOUGH2 at any time instant can be made during the MF runs at the end of a successful iteration for heat and moisture flow balances.

The new CFD model configuration in Case B eliminates the need for the equivalent dispersion coefficient, and thus offers several advantages. First, the dispersion coefficient is a flow, and not a fluid property, a time- and spatial-dependent function which varies from case-to-case. Second, only limited

dispersion coefficient data are available in the YM literature for the drift air space [7]. Third, there is no efficient method in sight other than solving first for real convection and post-processing the results to supplement dispersion coefficients for future model studies with various, new boundary and flow conditions in various emplacement drifts in any given emplacement panel at YM. Fourth, the effective, equivalent dispersion coefficient models such as in Cases A or C are simplifications that may be a low-order approximation of the convective transport mechanisms in the drift air space.

As mentioned before, the time- and space-dependent dispersion coefficient in Case C is back-calculated from the air flow fields derived from Case B. Similar to a method discussed in [7], the effective dispersion coefficients are defined by equating the convective moisture transport (based on the known air flow fields and moisture profiles along the drift) with an equivalent diffusive moisture transport (based on the known moisture gradient long the drift). This is done for various selected time steps and in each cross-section location i of the drift discretization:

$$qm_i = \rho_i D_i A_i \left.\frac{\partial \omega}{\partial x}\right|_i \tag{7}$$

Where qm_i is axial moisture flux at cross-section i, and

$\left.\dfrac{\partial w}{\partial x}\right|_i$ is vapor mass fraction gradient at cross-section i.

The axial moisture flux in Eq. (7) is calculated as the net, convective moisture flow in four air flow lines in the CFD model, either over, or inside the drip shield, as follows:

$$qm_i = \sum_{j=1}^{4} qa(j) \cdot \omega(j) \tag{8}$$

Where $qa(j)$ is air mass flow rate of jth air line at cross-section i, given as axial air flow velocity in each channel multiplied with the moist air density, and $\omega(j)$ is vapor mass fraction of jth air line at cross-

section *i*. Rearranging Eqs. (7) and (8) gives a simple expression for D_i as a function of known results from Case B.

In order to smoothen out the local fluctuations in the *D* caused by numerical derivation in $\partial\omega/\partial x$, we have tested the use of overall correlation equations that can represent the dispersion coefficients, separately for above and for under the drip shield air space. In previous work, we assumed that the dispersion coefficient correlated with an axial temperature difference over length in the form of a local Rayleigh number [15]. This time, we assume that the local temperature gradient is the main factor affecting the axial dispersion coefficient for both heat and moisture. We eventually selected the following correlation equation between the temperature gradient, $\partial T/\partial x$, local temperature, *T*, and axial dispersion coefficient, *D*, used for both heat and moisture as follows:

$$D_i = a \cdot (Ra_i)^b + c \tag{9}$$

Here, *a* and *b* are fitting parameters and *Ra* is modified Rayleigh number using the local axial temperature gradient at cross-section *i* as follows:

$$\left. \begin{array}{c} Ra_i = g \cdot \beta_i \cdot \left. \dfrac{\partial T}{\partial x} \right|_i \cdot \dfrac{d^4}{\alpha \cdot v} \\[2em] \beta_i = \dfrac{1}{T_i + 273.2} \end{array} \right\} \tag{10}$$

Where T is temperature at cross-section *i* , α is air thermal diffusivity, v is air kinematic viscosity, d is drift diameter, and g is 9.81 m/s². The constant *c* in Eq. (9) is a constant dispersion coefficient of 0.02 m²/s, an empirical value. Equation (9) is used to determine the *a* and *b* parameters against all D_i values defined in Eq. (7) by least-square fit. The fitting exercise uses 76 waste package locations along half of the drift length, assuming symmetry, and 21 time divisions over 5000 years, a total number of 1596 D_i values. The following error function is minimized:

$$\text{Fitting Error} = \sum_{1}^{1596} \left[D_i(\text{Eq 7}) - D_i(\text{Eq 9 with unknown } a \text{ and } b) \right]^2 = \min \qquad (11)$$

The two-dimensional minimization provides a and b values for all D_i values. The numerical results for under and over the drip shield air space will be discussed later in the paper.

COUPLED SIMULATION RESULTS

The simulation results for the drift wall temperature are shown in Fig. 2 for Cases A through C together for comparison along the emplacement drift length and at selected time periods. Likewise, Figs. 3 and 4 show the relative humidity and the condensate rate distributions, respectively.

The temperature results around the drift center from the new CFD configuration with an explicit in-drift air velocity solver in Case B agree well with the results from the dispersive model configuration in Cases A and C, but significant difference is seen in vapor pressure. Considerable differences between the model configurations in Cases A and B are also found in both temperature and vapor pressure at the cold end segments of the drifts. The large differences can be attributed to the strong, convective, naturally-driven, large-eddy air flow circulation in the axial direction of the drift. The results suggest that the new model in Case B is not only more realistic but it predicts more favorable storage conditions in the emplacement drift with less seepage and condensation (providing for less aqueous transport) and lower humidity (providing a less corrosive environment in general). For this reason, the MF model predicts no condensation in the emplacement area for several thousand years, while by contrast the condensation model described in [7] predicts small rates until approximately 3,000 years. Beyond 3,000 years, small rates in condensation appear in the MF model results, due to a decrease in efficiency of the axial, in-drift vapor transport which in turn leads to an increase in relative humidity. The in-drift environment at higher relative humidity and under a convective vapor influx from the rockmass into the still relatively hot mid-drift section shows small rates of condensation at some surface areas in Case B.

17

This may be explained by the complex, coupled boundary interactions, which include convective vapor fluxes between the in-drift and in-rock domains in the MF model.

The equivalent, effective dispersion model in Case C holds quite well against the convective model of Case B for both temperature and condensation distributions, and with only a slight disagreement in relative humidity along the heated drift section. This suggests that the time- and space-variant dispersion approach in Case C are more representative of the real air and moisture flow patterns along the drift than the uniform-value approach in Case A. The good agreement is, however, a circular success since the dispersion coefficient distribution is back-calculated directly from the convective model.

Further results from the new model solution are given for the natural, axial and cross-sectional air flows in the drift. The open air cross section of the emplacement drift is divided into eight segments, four over and four under the drip shields, forming eight longitudinal air distribution lines. The integrated-parameter CFD model for air flow applies 16 velocity components, eight along horizontal lines parallel with the drift axis and eight in the vertical plane, normal to the drift axis at each drift cross-section in the present model configuration. The velocity components and their positive directions are defined in Figures 5 and 6 for the air space above and under, respectively, the drip shields. These air flow velocity components are used for post-processing the equivalent dispersion coefficients, D, according to Eq. (7). Along a full drift, 454 x 18=8172 velocity components are determined from the integrated-parameter model calculation.

The MF model calculation results for the velocity components along the drift length are given in Figures 7 through 11 for various time instants during the post-closure time period up to 5,000 years. As shown, neither the horizontal nor the cross-sectional velocity components are constant along the drift length. The variation in the horizontal velocity components, $v_1^H \ldots v_8^H$, indicates that the recirculation loops are "leaky," that is, the flows are short-circuited with small bypass flows in the drift air space.

Nevertheless, the formation of a continuous, horizontal, large-scale eddy, half-drift length in size, is unmistakable.

Figure 12 is a schematic diagram of the dominant, averaged, natural axial air-recirculation loops in the air space inside and outside the drip shield. A simplified axial air flow pattern diagram is shown in Figure 13. Visualizing the air re-circulation loops as dominant flow patterns, one loop under and one over the drip shields, helps understanding the simulation results and the nature of the flow field.

No such axial air flow loops have been included in previous transport models for YM. The Natural Convection and Condensation studies conducted in [7] show dominantly cross-sectional, but no axial large-eddy flows, probably due to a much shorter drift length, and the very different boundary conditions used in the FLUENT CFD model. The open flow cross section in the drift is divided into unequal surface areas, A_i in the present model, therefore, the horizontal velocities do not sum to zero; however, the flow rates in each cross section strictly satisfy continuity, meaning that the inbound and outbound mass flow rates sum to zero.

The variation in the velocity components, v_1^V and v_8^V, of the cross-sectional circulation loops is especially strong along the drift length. The direction of the circulation reverses along the drift length perhaps multiple times, as indicated by the positive and negative signs of the velocity components, shown in Figures 7b through 11b. The ruggedness of the curves is caused by the disturbed cross-section and velocities in the gaps between the individual WPs.

The equivalent, effective dispersion coefficient is back-calculated from the simulation results of the moisture fluxes using Eqs. (7) and (8), and smoothened by fitting the overall fitting equations according to Eqs. (9)-(11). Figure 14, shows the results for above and under the drip shield for selected time periods. The maximum value of the dispersion coefficient according to fitting the convective model is about 1 m^2/s at early times, much higher than the value of 0.1 m^2/s given in the YM literature [7] as the

highest value. With time, as axial temperature gradients and convective transport patterns decrease in intensity, so do the dispersion coefficients. The highest dispersion coefficient along the drift are typically seen at the two ends of the emplacement sections of the drifts, consistent with the strong temperature gradients observed between the emplacement sections and the cool end sections of drifts.

The boundary conditions on the full drift surface in the MF model includes a rich variation of temperature and humidity, fully coupled and balanced with the in-rock TOUGH2 model. The natural driving force for the horizontal and vertical air circulations come from air density variations due to temperature and humidity changes. The change in the rotational direction of the vertical vertices along the drift length indicates that the air density change due to humidity variation becomes dominant over the change in air density due to temperature variation at the cold and humid drift sections. In a hot drift section, the vertical air circulation is expected to be dominantly temperature driven, causing upward air flow in the drift center. In a cold drift section with high relative humidity, the effect of vapor-content on the air density may overwhelm that of temperature. More humid and lighter air may rise over the drift wall and descend in the drift center, reversing the vertical circulation loop direction.

The simulation results suggest that large-eddy turbulent flow, as opposed to small-eddy flow, dominates the drift air space for at least 5000 years following waste emplacement. The size of the longitudinal eddy equals half of the drift length. The large-eddy flow structure apparent from the results in Case B appears to predict a much stronger axial heat and moisture transport than the dispersive model with 0.1 m^2/s used as the maximum value for YM. The large-eddy convective air flow makes the transport of heat and moisture from the high-temperature drift section to the colder, empty drift sections more active, helping to remove heat and moisture. These differences are important, since the conditions are drier in most of the drift sections where waste is emplaced and wetter in the end sections where no

waste is emplaced. The real transport mechanism by convection should be further explored and analyzed for the optimization of the design and the benefit of waste storage and isolation.

CONCLUSIONS

1. A fully-coupled, in-drift and near-field, in-rock model is configured and applied for the solution of a complex thermo-hydrologic-airflow problem at YM for a full emplacement drift, embedded in a mountain-scale rockmass with edge cooling.

2. The new model includes an explicit, natural air flow field solver within the drift air space during post-closure. From the new model, natural, buoyancy-driven air flow loops are predicted in both axial and vertical directions in a full emplacement drift. The new results are presented as Case B.

3. The new CFD model configuration explicitly models convective transport and eliminates the need for the input value of the equivalent dispersion coefficient, an artificial parameter that is a flow, and not a fluid property and is a time- and spatial-dependent function which varies from case-to-case. Only very limited dispersion coefficient data are available in the YM literature for the drift air space, and there is no efficient method in sight to supplement dispersion coefficients for future model studies other than that used in this paper. An equivalent dispersion coefficient distribution can be determined by post-processing an already existing simulation result, such as demonstrated in this paper.

4. Simulated results are given for temperature, humidity, and drift-wall condensation rates along the full length of an emplacement drift, using the new version of the MF model. The temperature and humidity data are roughly comparable to the 3D panel-scale validation results [6, 8, 9], with differences that would need to be evaluated carefully in light of the differences in the conceptual

models, boundary coupling of different domains, and mathematical implementations. Future modeling studies could benefit greatly from such an analysis.

5. The MF model predicts no drift-wall condensation in the emplacement area for several thousand years, then the onset of small rates at around 5,000 yrs. By contrast, the condensation model described in [7] predicts small rates until approximately 3,000 yrs, and no significant drift-wall condensation after that time. These differences likely stem from several factors, including the dispersive transport process model-elements to replace convection with dispersion, and boundary coupling between the in-drift and in-rock domains. Further studies are recommended with comparison between MF model results and appropriate field data.

6. The effective, equivalent dispersion coefficient model used in existing YM studies [e.g., 7] represents a low-order approximation of the convective transport mechanism in the drift air space. This conclusion is evidenced by comparing Cases B (with the convective model configuration results) to Case A (with the equivalent, effective dispersion coefficient derived from [7]). The theoretical bases of replacing convective transport with a dispersive one needs further studies, of which the presented work offers a first step. A new processing approach is presented for derivation of as time- and space-variant effective dispersion coefficient, and the results are used in Case C, giving quite acceptable agreement with Case B. However, Case C utilizes vapor transport results from Case B, and there is no guarantee that the constants of a and b in Eq. (9) are valid for an arrangement other than described in this paper.

7. Large-eddy turbulent flow, as opposed to small-eddy flow, seems to dominate the drift air space for at least 5000 years, as evidenced by the 3D velocity field distribution. The structure of such a flow field is not similar to one which is mixed by small-eddies; and, therefore, cannot be expected to support a convective, surrogate model.

8. The size of the longitudinal eddy equals half of the drift length for periods of time during post-closure. The large-eddy model in MF predicts a stronger axial heat and moisture transport than the equivalent dispersive model for the same arrangement from the thermally more active, high-temperature drift section to the colder, empty drift sections. The strong axial transport mechanism should be further explored and analyzed for the optimization of the design and the benefit of waste storage and isolation

REFERENCES

1. Danko, G., Walton, J., and Bahrami, D. 2008. *Increased Storage Capacity At Yucca Mountain Favors Thermal Management For A Cold Repository.* Journal of Nuclear Technology, July, Vol. 163, pp. 47-61.

2. Pruess, K., C. Oldenburg, and G. Moridis, 1999. *TOUGH2 User's Guide, Version 2.0.* Report LBNL-43134, Lawrence Berkeley National Laboratory, Earth Sciences Division, Berkeley, California.

3. Danko, G., 2008, *MULTIFLUX V5.0 Software Quantification Documents.* Software Tracking Number: 1002-5.0-00, Prepared for the Berkeley National Laboratory at University of Nevada, Reno.

4. Danko, G., 2006. *Functional or Operator Representation of Numerical Heat and Mass Transport Models*, *Journal of Heat Transfer*, February 2006, Vol. 128, 162-175.

5. Nitao, J. 2000. *NUFT, Flow and Transport code V3.0s.* Software Configuration Management, Yucca Mountain Project – STN: 10088-3.0S-00. Prepared at the Lawrence Livermore National Laboratory.

6. Bechtel SAIC Company, 2008. *Multiscale Thermohydrologic Model.* ANL-EBS-MD-000049, Rev. 03, Bechtel SAIC Company.

7. Bechtel SAIC Company, 2004. *In-drift natural convection and condensation.* Yucca Mountain Project Report, MDL-EBS-MD-000001 REV 00, Bechtel SAIC Company, Las Vegas, NV.

8. Birkholzer, J., N. Halecky, S.W. Webb, P.F. Peterson, G.S. Bodvarsson, 2006. *The Impact of Natural Convection on Near-Field TH Processes at Yucca Mountain.* Proceedings, 11th International High-Level Nuclear Waste Conference, April, Las Vegas, NV.

9. Birkholzer, J.T., Halecky, N., Webb, S.W., Peterson, P.F., Bodvarsson, G.S., 2008. *A Modeling Study Evaluating the Thermal-Hydrological Conditions in and Near Waste Emplacement Tunnels at Yucca Mountain*. Journal of Nuclear Technology, July, Vol. 163.

10. Hao, Y. Nitao, J.J., Buscheck, T.A. and Sun, Y., 2006. *Double Diffusive Natural Convection in a Nuclear Waste Repository*. Proceedings, 11th International High-Level Radioactive Waste Management Conference, Las Vegas, NV, pp. 615-622.

11. BSC 2001. *Natural Convection Calculation of Waste Package Drift Emplacement*. CAL-EBS-TH-000001 REV 00. Las Vegas, NV: BSC. ACC: MOL.2001108.0004.

12. Danko, G., Birkholzer, J., and Bahrami, D. 2008. *Coupled In-Rock and In-Drift Hydrothermal Model Study for Yucca Mountain*. Journal of Nuclear Technology, July, Vol. 163, pp. 110-128.

13. Welty, J. R., Wicks, C.E., and Wilson, R.E. 1984. *Fundamentals of Momentum, Heat, and Mass Transfer.* 3rd edition, Wiley and Sons, pp. 612-614, 360.

14. Danko G., Bahrami D., Birkholzer J. 2008. *Comparison of Axial Convection and Equivalent Dispersion Models in Emplacement Drifts*. Proceedings, 12th International High-Level Radioactive Waste Management Conference, Las Vegas, NV, pp. 299-307.

15. Danko G., Bahrami D., Birkholzer J. 2006. *The Effect of Unheated Sections on Moisture Transport in the Emplacement Drift*. Proceedings, 11th International High-Level Radioactive Waste Management Conference, Las Vegas, NV, pp. 1-8.

FIGURES
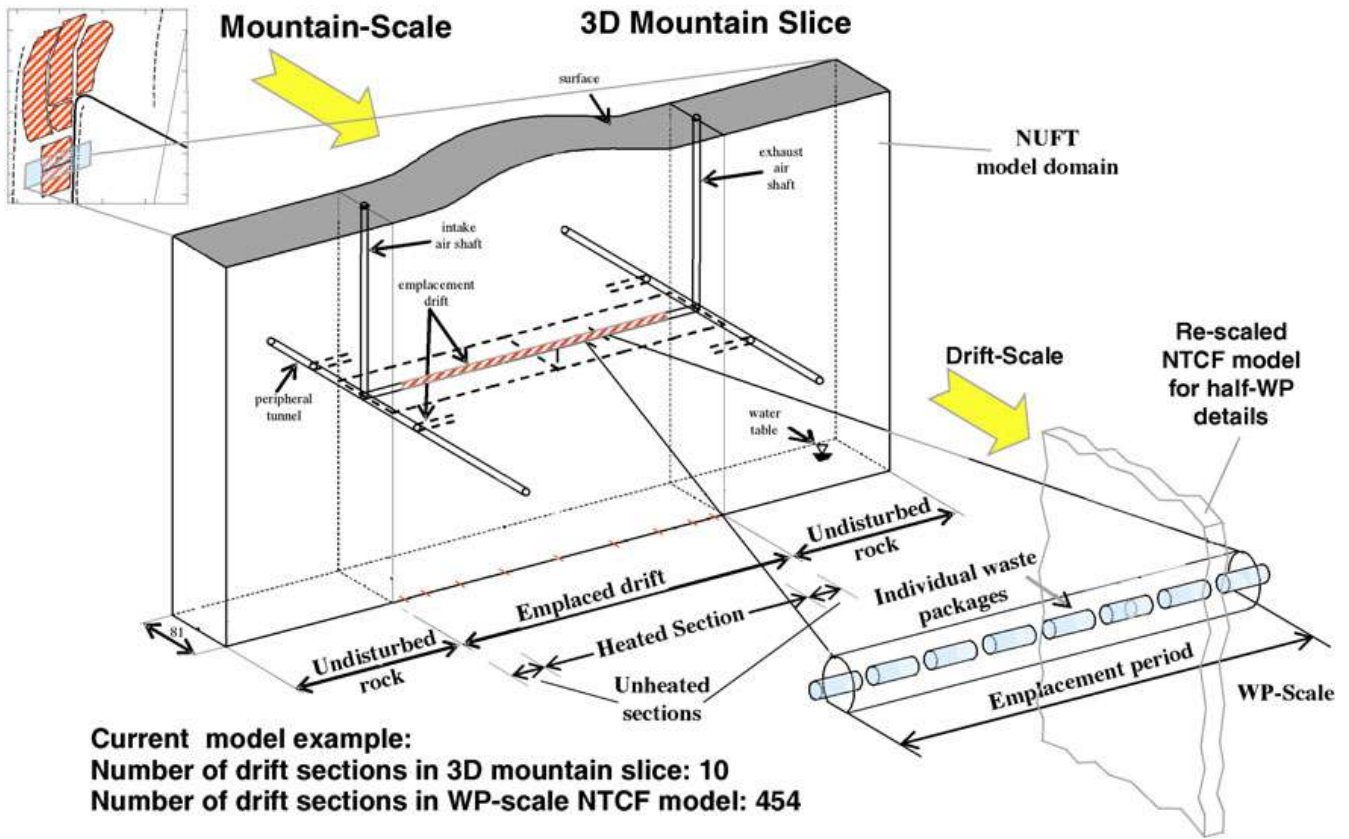
Figure 1. Multi-scale, in-rock and in-drift model domains (From Danko, et al., 2008 [1])
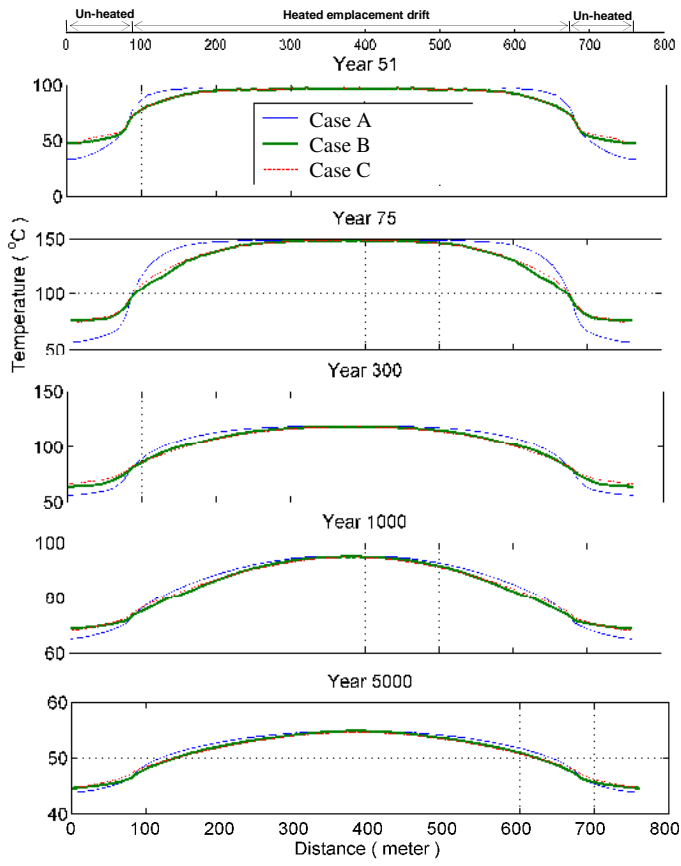
Figure 2. Drift invert temperature variation with drift length at selected post-closure time periods.
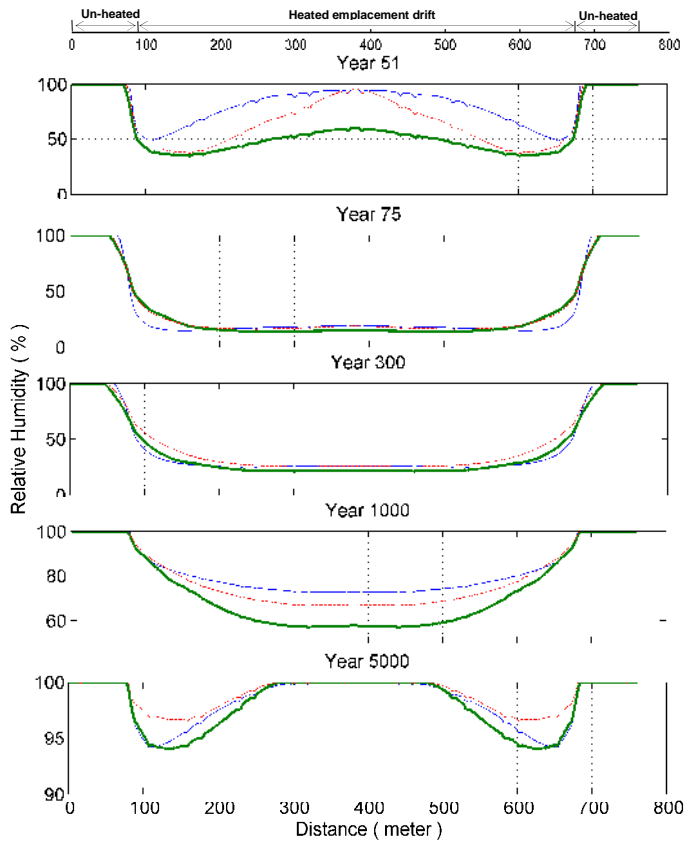
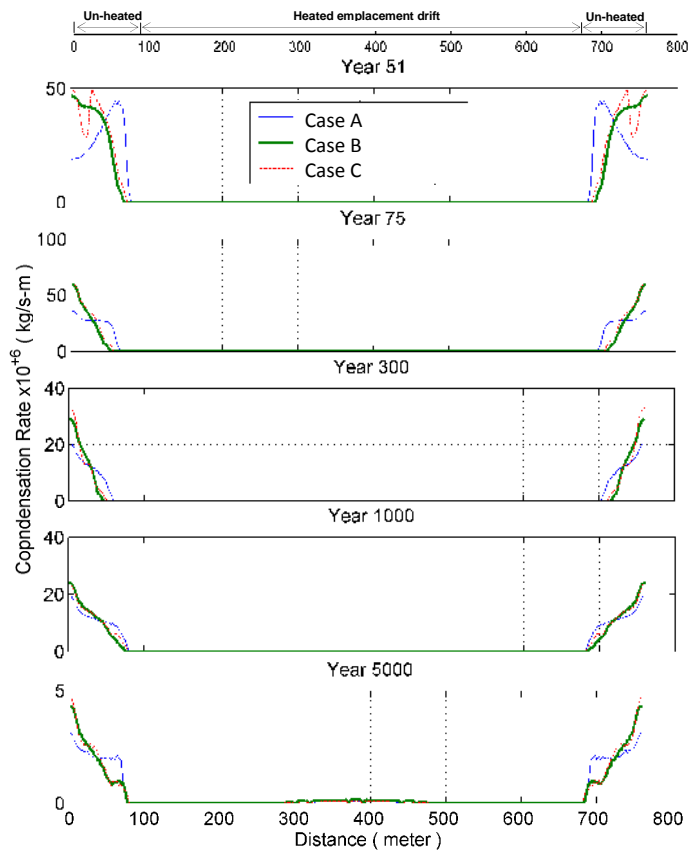Figure 3. Drift invert relative humidity variation with drift length at selected post-closure time periods.

Figure 4. Drift condensation flux variation with drift length at selected post-closure time periods.
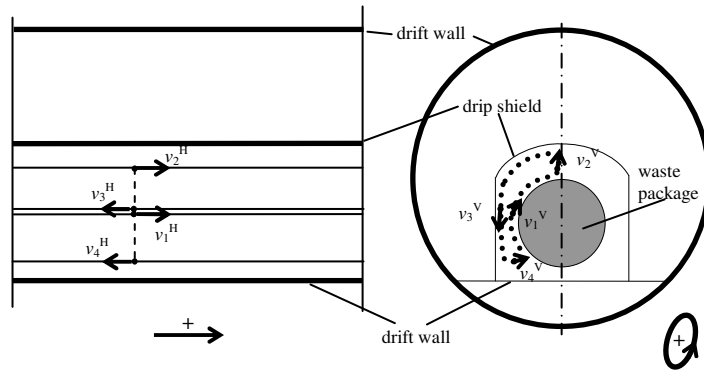
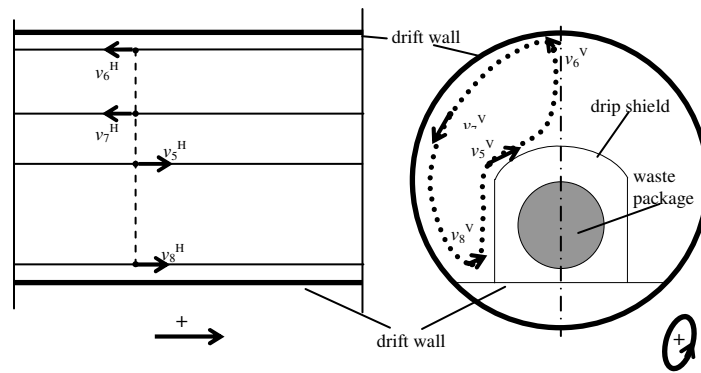Figure 5. Definition of velocity components at a given cross section under the drip shield

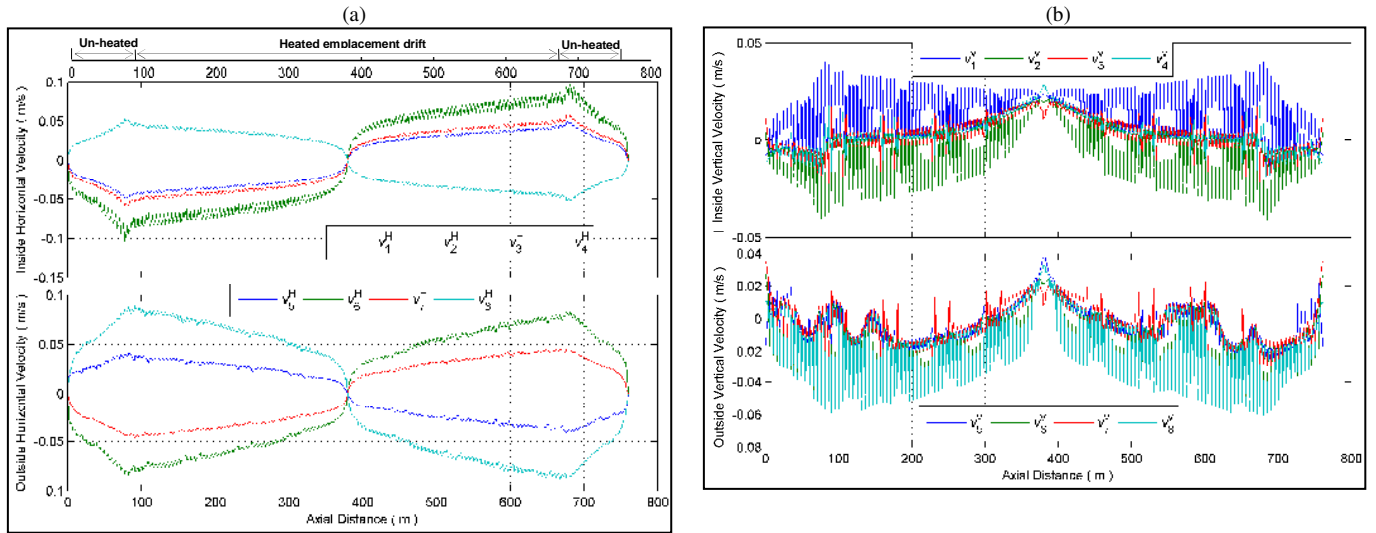Figure 6. Definition of velocity components at a given cross section outside the drip shields.
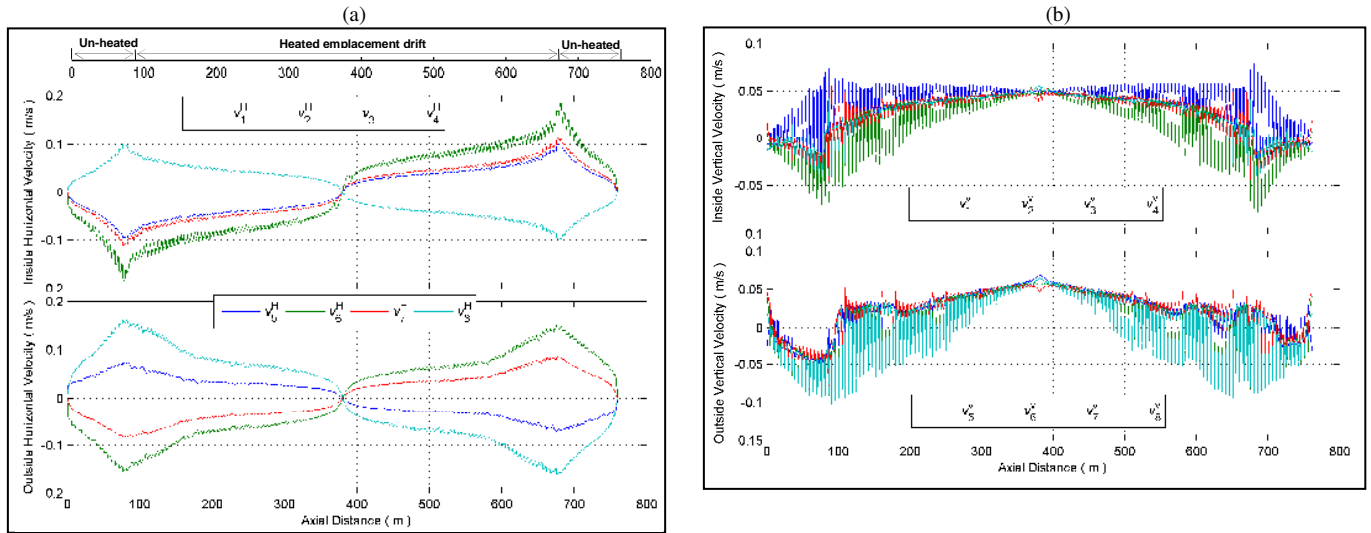
Figure 7. Spatial distribution of the axial (horizontal) (a) and cross-sectional (vertical) (b) velocity

components along eight air streams outside and inside the drip shield air spaces at Year 51 after waste

emplacement.
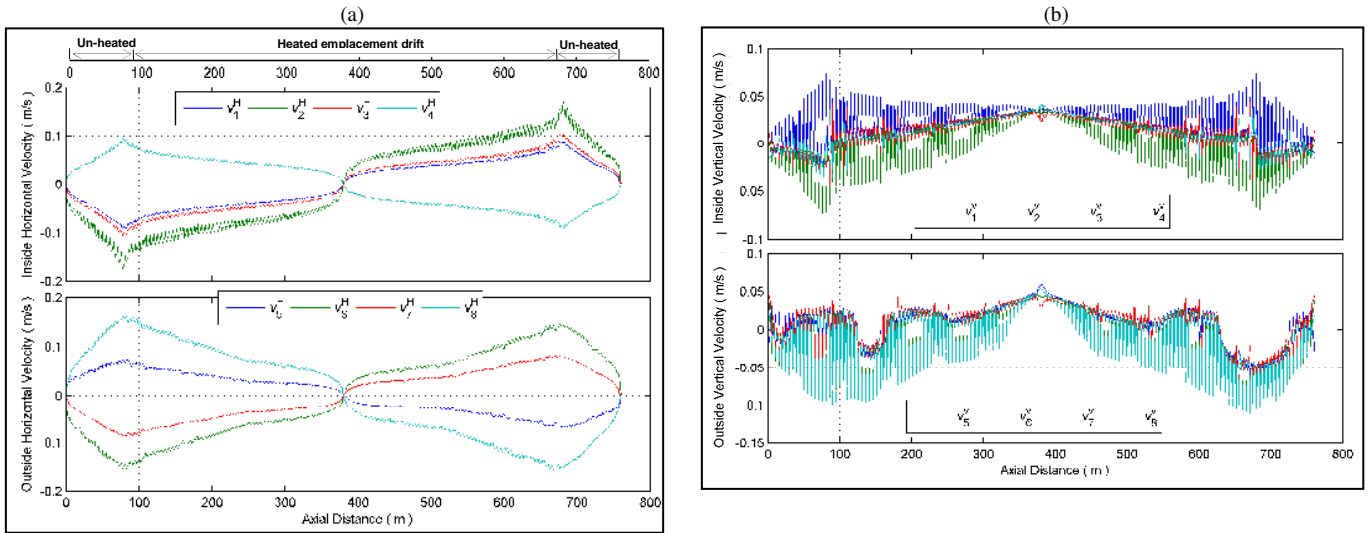
Figure 8. Spatial distribution of the axial (horizontal) (a) and cross-sectional (vertical) (b) velocity components along eight air streams outside and inside the drip shield air spaces at Year 75 after waste emplacement.
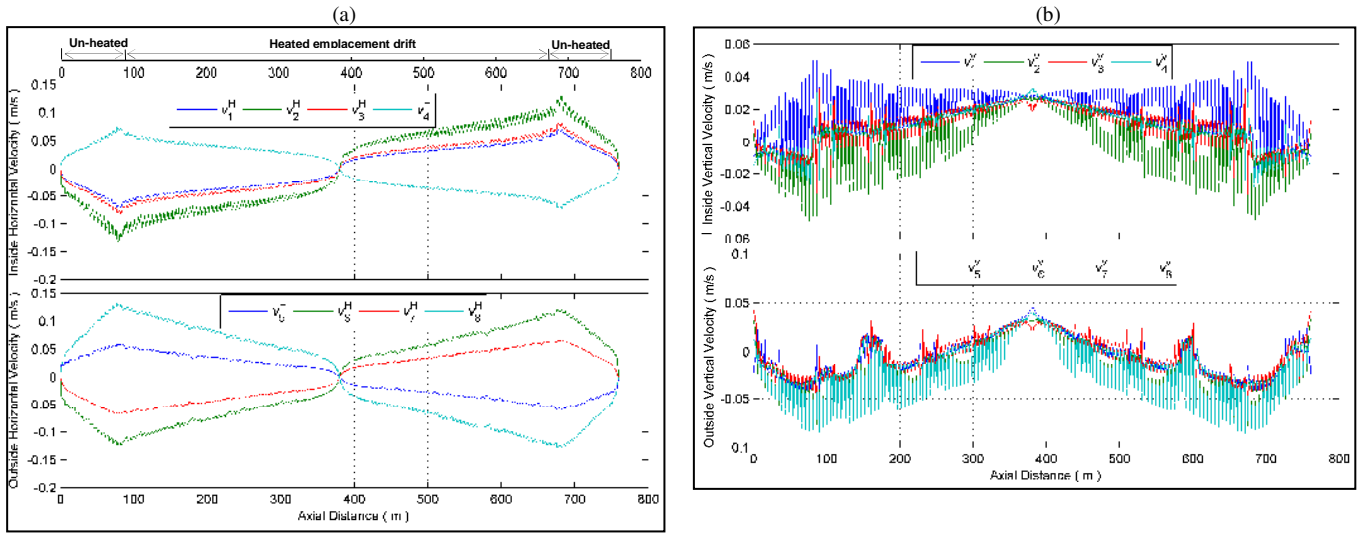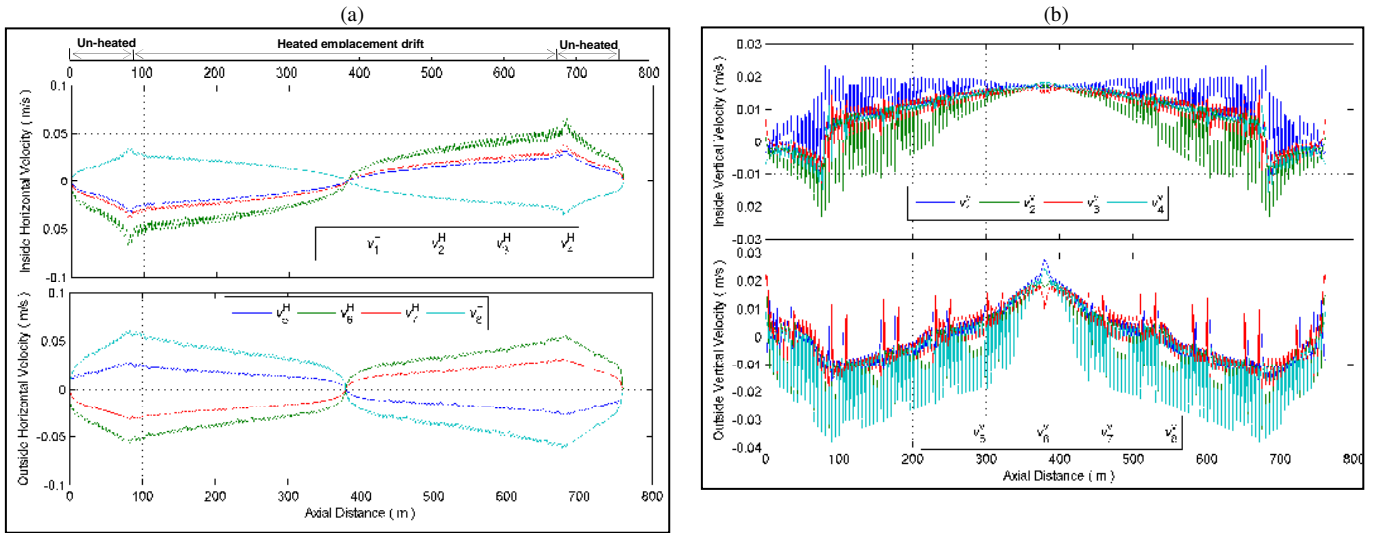
Figure 9. Spatial distribution of the axial (horizontal) (a) and cross-sectional (vertical) (b) velocity components along eight air streams outside and inside the drip shield air spaces at Year 300 after waste emplacement.

Figure 10. Spatial distribution of the axial (horizontal) (a) and cross-sectional (vertical) (b) velocity components along eight air streams outside and inside the drip shield air spaces at Year 1000 after waste emplacement.
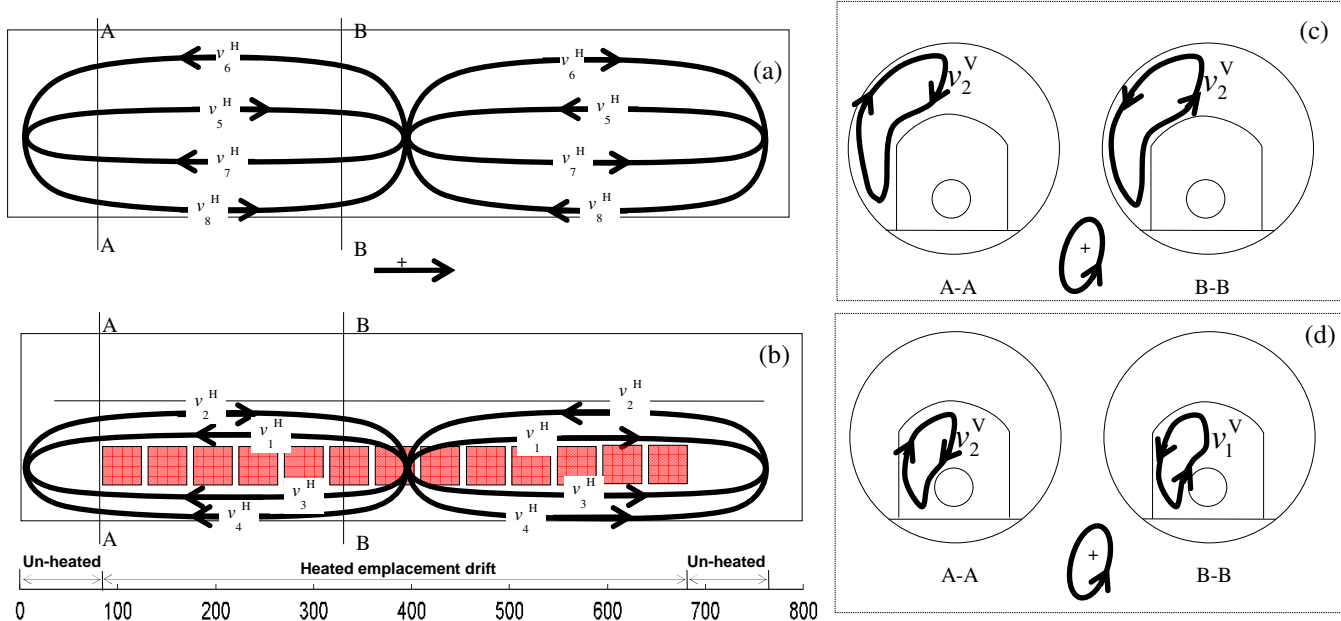
Figure 11. Spatial distribution of the axial (horizontal) (a) and cross-sectional (vertical) (b) velocity components along eight air streams outside and inside the drip shield air spaces at Year 5000 after waste emplacement.

Figure 12. Schematic diagram of the natural, axial air-recirculation loops over (a); and under(b) drip

shields. Cross-sectional air flow loops over(c); and under(d) drip shields at two locations along the drift
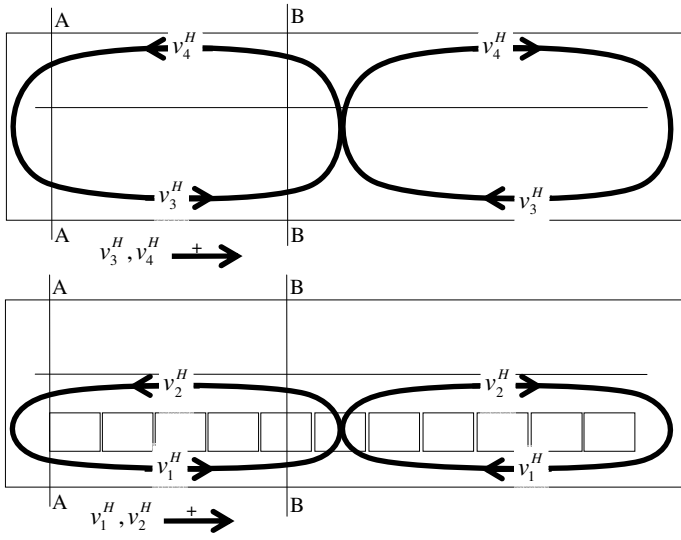
are also shown.

Figure 13. Dominant, averaged, drift-scale natural air flow patterns in one emplacement drift.
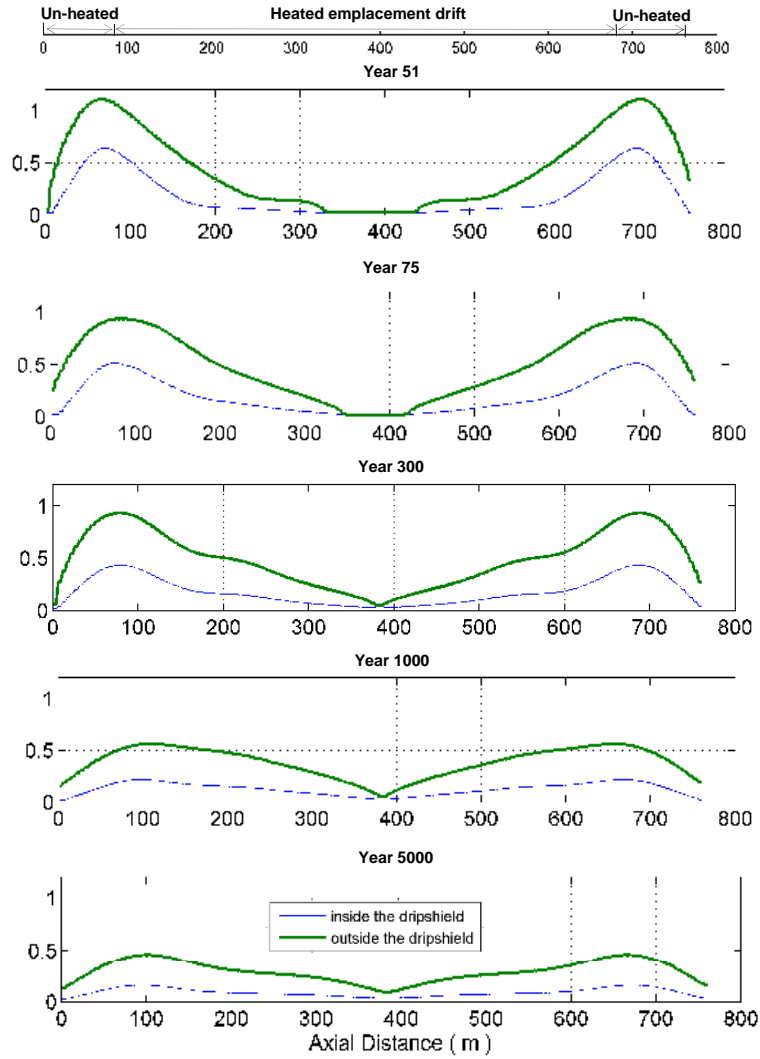
Figure 14. Axial, equivalent moisture dispersion coefficient at selected post-cloosure time divisions, back-calculated from the convective transport model in Case B.